Computational Materials Science 50 (2011) 2397–2410

Contents lists available at ScienceDirect

Computational Materials Science

journal homepage: www.elsevier.com/locate/commatsci

Modelling of particle nucleation and growth in binary alloys under elastic deformation: An application to a Cu–0.95 wt%Co alloy

D. den Ouden [a,b,c,*], F.J. Vermolen [b], L. Zhao [a,c], C. Vuik [b], J. Sietsma [c]

[a] Materials innovation institute, Mekelweg 2, P.O. Box 5008, 2600 GA Delft, The Netherlands
[b] Delft University of Technology, Delft Institute of Applied Mathematics, Mekelweg 4, 2628 CD Delft, The Netherlands
[c] Delft University of Technology, Materials Science and Engineering, Mekelweg 2, 2628 CD Delft, The Netherlands

ARTICLE INFO

Article history:
Received 18 October 2010
Received in revised form 14 February 2011
Accepted 22 February 2011
Available online 8 April 2011

Keywords:
KWN-model
Nucleation
Cu–Co system
Elastic deformation
Finite-element simulations

ABSTRACT

This study incorporates the effect of elastic deformation in a previously proposed model for the nucleation and growth of precipitates. We adapt the KWN-model by Robson [20] to incorporate the effect of strain energy arising from elastic deformation on the homogeneous nucleation and growth of Co particles in a Cu–Co system at constant temperatures. The finite-volume method is used for the KWN-model and the finite-element method is used to simulate elastic deformations within a cylindrical tension test specimen. Simulations of the nucleation and growth of Co particles in a Cu–Co system on the cylindrical region show that the incorporation of elastic strain energies has a noticeable impact on the process. The derived quantities of homogeneous nucleation and growth, such as the particle volume fraction and the particle number density, show a clear spatial correlation with the calculated strain energy. The results also show that the currently presented algorithm, which incorporates the influence of elastic deformation, has low computational cost with respect to full simulations, with just a minimal loss of accuracy.

1. Introduction

Metalworking of alloys is a complex operation that involves several aspects, such as dislocation movement, grain recrystallization and secondary phase precipitation, that influence the usability of the object. The influence of these aspects has been studied and documented by a process of trial and error. An analytical approach to investigate these aspects could verify the obtained experimental results and extend the knowledge about the behavior of alloys during metalworking.

During the last two decades various models for the nucleation and growth of precipitates in alloys have been proposed and evaluated. These models can be divided into four categories. The first category concerns models which predict the effect of nucleation and growth of precipitates on the evolution of a particle size distribution function. A classical example of this model is the KWN-model by Kampmann and Wagner [14], which has been extended and evaluated by, amongst others, Robson [20]. The second category consists of models that predict the nucleation and growth of precipitates using a mean variable approach, which model the time evolution of variables such as the mean particle radius and the particle number density. An example of such a model has been proposed by Deschamps and Brechet [8]. The third category contains models that predict the growth and dissolutions of precipitates present in a system by solving Stefan-like problems for different precipitate sizes. One of the latest models in this area is developed by Vermolen et al. [29]. Finally a category containing models which describe precipitation dynamics using statistical methodologies can be identified, such as the model by Soisson et al. [25]. We will focus in this article on the KWN-model, as this model can predict both nucleation, growth and coarsening of precipitates with a high accuracy and level of detail, without resorting to artificial couplings between the separate physical phenomena.

This article will present an adapted KWN-model for homogeneous nucleation and growth of particles by Robson's formalism [20]:

- Which incorporates more physical effects.
- Which incorporates the effect of elastic deformations.

These goals will be achieved by reducing the number of empirical parameters and introducing strain energy terms. The elastic deformations will be modelled using standard linear elastic models in cylindrical coordinates, see for example Jaeger et al. [13] and Chau and Wei [7]. Furthermore a numerical algorithm will be presented to simulate the influence of the elastic deformations on the nucleation and growth of precipitates, which decreases the computational cost significantly without a high loss of accuracy.

* Corresponding author at: Materials Innovation Institute, Mekelweg 2, P.O. Box 5008, 2600 GA Delft, The Netherlands. Tel.: +31 152787297.
E-mail addresses: d.denouden@m2i.nl (D. den Ouden), F.J.vermolen@tudelft.nl (F.J. Vermolen), Lie.Zhao@tudelft.nl (L. Zhao), C.Vuik@tudelft.nl (C. Vuik), J.Sietsma@tudelft.nl (J. Sietsma).

0927-0256/$ - see front matter © 2011 Elsevier B.V. All rights reserved.
doi:10.1016/j.commatsci.2011.02.044

In the present work we will first present the models for the elastic deformations, and for the nucleation and growth of precipitates, after which the models will be discretized using a finite-element method for the model for elastic displacements and finite-volume methods for the nucleation model. Thereafter the mentioned algorithm for simulating the influence of the elastic displacements on the nucleation and growth of precipitates will be discussed. The models and algorithm will be demonstrated by an application to a Cu–0.95 wt%Co alloy, similar to the application by Robson [20], as for this alloy it is known to a fair extent that primarily homogeneous nucleation of precipitates occurs. Next the results of the influence of a tensile strain on a specimen will be given and a discussion on the influence of the temperature and the interface energy will be presented.

2. The model

The nucleation and growth of precipitates are modelled by the KWN-model from Robson [20]. We present an extensive discussion of this model. The main features of the KWN-model are:

- All particles are spherical and classified by their radius in meters (m). In this paper, we assume that the precipitates are much harder than the matrix, which causes the shape of the particles to remain spherical during elastic deformation.
- The time behavior in seconds (s) of the model is described by the partial differential equation:

$$\frac{\partial N}{\partial t} = -\frac{\partial [N v]}{\partial r} + S, \tag{1}$$

in which $N \equiv N(r,t)$ in m^{-3} represents the number density of particles with radius r and at time t, $v \equiv v(r,t)$ in $\mathrm{m\,s}^{-1}$ represents the growth rate of particles with radius r and at time t and $S \equiv S(r,t)$ in $\mathrm{m}^{-3}\,\mathrm{s}^{-1}$ represents a source function representing the number of new particles with radius r and at time t per second. v will be defined in Section 2.2.2.
- The value of the source function S is calculated from classical nucleation theory (CNT) and is given by

$$S(r,t) = \begin{cases} I(t) & \text{if } r \in [r^*(t), 1.05 r^*(t)], \\ 0 & \text{otherwise.} \end{cases} \tag{2}$$

Here $I \equiv I(t)$ is the nucleation rate of the particles following from CNT and $r^* \equiv r^*(t)$ the critical radius following from CNT. The value 1.05 is adopted from Myhr and Grong [15]. Both I and r^* will be defined in Section 2.2.1.
- To Eq. (1) the well known first-order upwind method is applied, combined with a time integration method.

In this paper, we couple the KWN-model with a model for elastic deformations.

2.1. Elastic deformation

In the present paper we will only model the theoretical influence of elastic deformation in a cylindrical tension specimen on the process of nucleation and growth of particles, but the concept can in principle be extended to regions with different geometries. The concept of elastic deformation will be simplified under the assumptions of local isotropy, instantaneous displacement, rotation symmetry around the central axis and that a formulation of the model for elastic deformations in cylindrical coordinates (η, θ, z) is possible. The symbol η represents the radial coordinate in cylindrical coordinates, as r has been defined as the precipitate radius. θ and z represent the azimuthal coordinate respectively the height coordinate in cylindrical coordinates. The latter two assumptions immediately impose restrictions on the formulation of the model. Rotation symmetry implies that at the central axis no radial displacements can occur. This yields the boundary condition

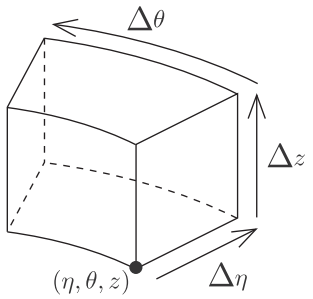

Fig. 1. Cylindrical element at (η, θ, z).

$$u_\eta(0,\theta,z) = 0. \tag{3}$$

Furthermore, the assumptions indicate that all displacements are constant with respect to the azimuthal direction θ, i.e. $\frac{\partial}{\partial\theta}(\cdot) = 0$, and that in the azimuthal direction no displacements occur, i.e. $u_\theta = 0$, at any point in the material.

Consider a cylindrical region with an infinitely small element of this region. This element is of the form as in Fig. 1. Applying a simple balance of forces in the axial and radial direction and taking the appropriate limits, we arrive at the following system of equations on the domain Ω [13]

$$-\frac{\partial \sigma_{\eta\eta}}{\partial \eta} - \frac{\partial \sigma_{\eta z}}{\partial z} - \frac{\sigma_{\eta\eta} - \sigma_{\theta\theta}}{\eta} = 0, \tag{4a}$$

$$-\frac{\partial \sigma_{\eta z}}{\partial \eta} - \frac{\partial \sigma_{zz}}{\partial z} - \frac{\sigma_{\eta z}}{\eta} = 0. \tag{4b}$$

Here the stress $\sigma_{\alpha\beta}$ acts on a plane normal to the β direction in the direction α.[1] Due to the assumption of rotational symmetry no force balance for the azimuthal direction is needed.

By the assumption of local isotropy, we can model the relationship between the stresses and strains using Hooke's Law:

$$\sigma_{\alpha\beta} = \delta_{\alpha\beta}\lambda_m(\varepsilon_{\eta\eta} + \varepsilon_{\theta\theta} + \varepsilon_{zz}) + 2\mu_m\varepsilon_{\alpha\beta} \quad \alpha,\beta \in \{\eta,\theta,z\}, \tag{5}$$

where λ_m is Lamé's first parameter, μ_m the shear modulus of the material, $\underline{\underline{\varepsilon}} = (\varepsilon_{\alpha\beta})_{\alpha,\beta\in\{\eta,\theta,z\}}$ the strain tensor and $\delta_{\alpha\beta}$ the Kronecker delta. The parameters λ,μ are calculated from the materials constants ν_m, the Poisson's ratio, and the bulk modulus K_m. The Poisson's ratio is assumed independent of temperature [21], whereas the bulk modulus is modelled with temperature dependency as $K_m = K_m^0 - K_m^1 \cdot T$ [6] under the assumption that the elastic properties of copper are representative for the entire specimen under elastic deformation.

The strains are in turn related to the displacements in the radial and axial direction, being (u_η, u_z), as [7]:

$$\varepsilon_{\eta\eta} = \frac{\partial u_\eta}{\partial \eta}, \qquad \varepsilon_{\theta\theta} = \frac{u_\eta}{\eta}, \qquad \varepsilon_{zz} = \frac{\partial u_z}{\partial z}, \qquad \varepsilon_{\eta z} = \frac{1}{2}\left(\frac{\partial u_\eta}{\partial z} + \frac{\partial u_z}{\partial \eta}\right). \tag{6}$$

Besides the partial differential equations defined in Eq. (4), boundary conditions for both u_η and u_z should be defined. Let the boundary Γ of Ω consist of four regions $\Gamma_{\mathrm{ess},\,\eta}$,$\Gamma_{\mathrm{nat},\eta}$, $\Gamma_{\mathrm{ess},z}$ and $\Gamma_{\mathrm{nat},z}$, where " ess" refers to essential boundary conditions, "nat"

[1] These stresses are symmetric, so the location of α and β in the definition can be switched.

to natural boundary conditions and η,z refer to the direction on which the boundary conditions act. For these subboundaries we have:

$$\begin{aligned} &\Gamma_{\mathrm{ess},\eta} \cup \Gamma_{\mathrm{nat},\eta} = \Gamma, \qquad \Gamma_{\mathrm{ess},z} \cup \Gamma_{\mathrm{nat},z} = \Gamma, \\ &\Gamma_{\mathrm{ess},\eta} \cap \Gamma_{\mathrm{nat},\eta} = \emptyset, \qquad \Gamma_{\mathrm{ess},z} \cap \Gamma_{\mathrm{nat},z} = \emptyset. \end{aligned} \tag{7}$$

Then we can define the following boundary conditions:

$$u_\eta = u_\eta^* \quad \text{for } (\eta,z) \in \Gamma_{\mathrm{ess},\eta}, \tag{8a}$$

$$\left(\underline{\underline{\boldsymbol{\sigma}}} \cdot \boldsymbol{n}\right)_\eta = f_\eta \quad \text{for } (\eta,z) \in \Gamma_{\mathrm{nat},\eta}, \tag{8b}$$

$$u_z = u_z^* \quad \text{for } (\eta,z) \in \Gamma_{\mathrm{ess},z}, \tag{8c}$$

$$\left(\underline{\underline{\boldsymbol{\sigma}}} \cdot \boldsymbol{n}\right)_z = f_z \quad \text{for } (\eta,z) \in \Gamma_{\mathrm{nat},z}, \tag{8d}$$

in which u_η^*, u_z^* are predefined displacements along the essential boundaries and f_η, f_z are predefined forces along the natural boundaries.

After solving the system given by Eqs. (4) and (8), the elastic strain energy density Δg_s^{el} present in the system at any point is calculated, using the formula:

$$\Delta g_s^{el} = \frac{1}{2}\underline{\underline{\boldsymbol{\sigma}}} : \underline{\underline{\boldsymbol{\varepsilon}}}, \tag{9}$$

in which : represents the Frobenius inner product, defined for two $n \times m$ matrices A and B as:

$$A : B = \sum_{i=1}^{n}\sum_{j=1}^{m} A_{ij}B_{ij}. \tag{10}$$

2.2. Nucleation and growth of precipitates

This section will describe the models for nucleation and growth of precipitates, which is based on the model by Robson [20]. The changes with respect to this model will be discussed.

2.2.1. Nucleation

Robson [20] assumes that the time-dependent homogeneous nucleation rate I, as used in Eq. (2), is given by

$$I = N_v Z \beta^* \exp\left[-\frac{\Delta G^*}{kT}\right] \exp\left[-\frac{\tau}{t}\right], \tag{11}$$

where k, T and t represent the Boltzmann constant, the temperature, respectively the time. Furthermore, N_v is the number of potential homogeneous nucleation sites per unit volume, Z the Zeldovich factor, β^* the frequency of atomic attachment to a growing particle and τ the incubation time for homogeneous nucleation. The term ΔG^* is the free energy barrier for homogeneous nucleation which must be overcome before precipitation occurs. Using the assumption of all precipitates being spherical, the three variables Z, β^*, τ can be expressed by [20]:

$$Z = \frac{V_a^p\sqrt{\gamma}}{2\pi\sqrt{kT}}\left(\frac{1}{r^*}\right)^2, \tag{12a}$$

$$\beta^* = \frac{4\pi D x_m}{(a_p)^4}(r^*)^2, \tag{12b}$$

$$\tau = \frac{2}{\pi Z^2 \beta^*}. \tag{12c}$$

In these formulas V_a^p is the atomic volume of the precipitate, r^* the critical radius of precipitation, γ the particle/matrix interface energy, D the bulk diffusion coefficient of the solute [10], calculated with the Arrhenius relation, x_m the atomic fraction of solute in the matrix and a_p the lattice constant of the precipitate. The values for the parameters in this system are given in Table 1.

Table 1
Used parameter values.

Parameter	Unit	Value	Comments
a_m^0	m	3.6027×10^{-10}	Hahn [11], Straumanis and Yu [27]
a_m^1	m/K	1.5788×10^{-15}	Hahn [11], Straumanis and Yu [27]
a_m^2	m/K^2	1.1854×10^{-17}	Hahn [11], Straumanis and Yu [27]
a_m^3	m/K^3	-1.1977×10^{-20}	Hahn [11], Straumanis and Yu [27]
a_m^4	m/K^4	5.3276×10^{-24}	Hahn [11], Straumanis and Yu [27]
a_p^0	m	3.5249×10^{-10}	Owen and Madoc Jones [17]
a_p^1	m/K	3.9540×10^{-15}	Owen and Madoc Jones [17]
a_p^2	m/K^2	7.2209×10^{-19}	Owen and Madoc Jones [17]
D_0	m^2/s	4.3×10^{-5}	Döhel et al. [10]
K_m^0	N/m^2	1.4652×10^{11}	Chang and Hultgren [6]
K_m^1	N/m^2 K	4.0243×10^{7}	Chang and Hultgren [6]
μ_p^0	N/m^2	9.3486×10^{10}	Betteridge [4]
μ_p^1	N/m^2 K	4×10^{7}	Betteridge [4]
ν_m		0.35	Rolnick [21]
ν_p		0.32	Betteridge [4] [4]
p_0^e		2.853	Servi and Turnbull [24]
p_1^e	K	2.875	Servi and Turnbull [24]
Q_d	J/mol	214×10^3	Döhl et al. [10]
x_p		1	Assumed

In the classical nucleation theory, the free energy change due to a homogeneous nucleation event, ΔG, is assumed [18] to be of the form

$$\Delta G = -\frac{4}{3}\pi r^3(\Delta g_v - \Delta g_s^m) + 4\pi r^2\gamma, \tag{13}$$

for spherical particles, of which the derivative with respect to r is equated to zero and solved for r to find the critical radius r^* and the corresponding free energy barrier for homogeneous nucleation ΔG^*. In this formula Δg_v is the chemical volume free energy density and Δg_s^m the misfit strain energy density, both with positive sign. We adapt this formula by assuming that the free energy due to homogeneous nucleation of a precipitate with radius r is reduced due to the release of elastic strain energy in the matrix. Assuming the elastic strain energy density Δg_s^{el} to be known using the model described in the previous section (see Eq. (9)), the free energy ΔG can be described by:

$$\Delta G = -\frac{4}{3}\pi r^3(\Delta g_v - \Delta g_s^m + \Delta g_s^{el}) + 4\pi r^2\gamma. \tag{14}$$

Differentiation with respect to r and equating to zero gives the modified critical radius

$$r^* = \frac{2\gamma}{\Delta g_v - \Delta g_s^m + \Delta g_s^{el}}, \tag{15}$$

with the corresponding homogeneous nucleation energy barrier

$$\Delta G^* = \frac{4}{3}\pi\gamma(r^*)^2. \tag{16}$$

Following Aaronson et al. [1] and assuming a dilute solution approximation, the volume free energy density can be expressed by

$$\Delta g_v = \frac{RT}{V_m^p}\left(x_p \ln\left(\frac{x_m}{x_m^e}\right) + (1-x_p)\ln\left(\frac{1-x_m}{1-x_m^e}\right)\right), \tag{17}$$

where V_m^p is the molar volume of the precipitate, x_p the molar fraction of the solute in the precipitate, x_m^e the equilibrium molar fraction of the solute in the matrix for spherical precipitates [24][2] and R the gas constant. Note that the original derivation of Eq. (17) by Aaronson et al. [1] is based on a binary system. Investigation of

[2] $\log_{10} C_m^e = p_0^e - p_1^e/T \times 10^3$, the equilibrium concentration in wt% from which x_m^e can be determined.

the change in x_m^e due to an increase of the Gibbs energy of the matrix by amounts similar as in Table 3 and the effect on the simulations have shown that x_m^e exhibits a relative change of 2×10^{-3} and the simulation results are therefore not significantly affected. Obtaining the Gibbs energy is done by the use of the TCEF6 database of Thermo-Calc Software AB [28]. We can conclude that the influence of Δg_s^{el} on the value of x_m^e is negligible for the application in this research.

The misfit strain energy density Δg_s^m is given by

$$\Delta g_s^m = 3\varepsilon_m^2 \delta_p \left[1 - \left(1 + \frac{\delta_m}{\delta_p}\left(\frac{3(1-\nu_m)}{1+\nu_m} - 1\right)\right)^{-1}\right], \tag{18}$$

for a coherent spherical particle, following Barnett et al. [3]. Here ν_m,ν_p are the Poisson's ratios of the matrix and the precipitate, and where δ_m, δ_p are constants related to the Poisson's ratios ν_m, ν_p and the shear modulus of the matrix μ_m and particle μ_p:

$$\delta_m = \mu_m \frac{1+\nu_m}{1-2\nu_m}, \qquad \delta_p = \mu_p \frac{1+\nu_p}{1-2\nu_p}. \tag{19}$$

The misfit strain ε_m represents the linear strain due to the misfit between the lattices of the matrix and precipitate if a linear interphase is assumed and can be expressed as [19]

$$\varepsilon_m = \frac{a_p - a_m}{a_m}, \tag{20}$$

in which a_m and a_p are the lattice parameter of the matrix respectively the precipitate. The shear modulus μ_p is modelled with a linear temperature dependence as $\mu_p = \mu_p^0 - \mu_p^1 \cdot T$ following data from Betteridge [4]. The lattice parameter a_p is modelled using data from Owen and Madoc Jones [17] as $a_p = a_p^0 + a_p^1 T + a_p^2 (T)^2$ and the lattice parameter a_m is modelled by combining data from Straumanis and Yu [27] and Hahn [11] as $a_m = a_m^0 + a_m^1 T + a_m^2 (T)^2 + a_m^3 (T)^3 + a_m^4 (T)^4$. For the physical properties of the matrix respectively the precipitate it is assumed that the properties of copper respectively cobalt are representative.

On the value of N_v, the number of potential homogeneous nucleation sites per unit volume, see Eq. (11), various theories exist. One of the earliest theories by Russell [22] proposed to use the total number of atoms per unit volume in the matrix. Robson [20] suggests that using the number of solute atoms per unit volume in the matrix, i.e. the value from Russell [22] multiplied by the molar fraction of solute, gives a better agreement between predicted and measured results. Robson [20] also suggests using the molar fraction of solute as an empirical parameter to match predicted and measured results. Instead of using the molar fraction as an empirical parameter, we suggest the following formula for the number of potential homogeneous sites N_v

$$N_v = \frac{N_v^R x_m}{N_a^*}, \tag{21}$$

where N_v^R is the total number of atoms per unit volume in the matrix and N_a^* the number of atoms in a critical particle. We suggest this adaptation, as we believe from a theoretical point of view that the number of potential homogeneous nucleation sites is equal to the maximum number of nuclei that can form in a system, as any number higher is unphysical. This means that if N_v^R is the total number of atoms per cubic meter, $N_v^R x_m$ atoms of the solute are present. Only one out of every N_a^* atoms can form the basis of a nucleus, as each nucleus contains N_a^* atoms. This leads to Eq. (21). The value of N_a^* is approximated by calculating the number of unit cells of the particle phase that fit within a particle with critical radius r^* and subsequently by multiplying this quantity by the number of Co atoms within a unit cell of the particle phase. During simulations it has been seen that the number of potential homogeneous nucleation sites N_v initially has a value in the range of 10^{25}–10^{26} m^{-3} which decreases to zero due to depletion of Co atoms in the matrix at the end of the simulation and the critical radius to become zero.

2.2.2. Growth

In the previous section the nucleation rate I has been discussed, which is incorporated in the source function S of Eq. (1). The other factor influencing the time evolution of the particle distribution is the growth rate v. Following Robson [20], we set

$$v = \frac{D}{r}\frac{C_m - C_m^r}{C_p - C_m^r}, \tag{22}$$

in which C_m^r is the concentration of solute in the matrix at the particle/matrix interface, C_m the mean concentration of solute in the matrix and C_p the concentration of solute in the precipitate, all in weight percentages. The value of the concentration C_m^r is modelled by an application of the Gibbs–Thomson equation

$$C_m^r = C_m^e \exp\left(\frac{2\gamma V_m^p}{RT}\frac{1}{r}\right). \tag{23}$$

At this moment we assume that the value of the particle/matrix interface energy γ is the same for both the growth of particles as the nucleation of particles, which is in line with Robson [20].

If we set $v(r,t)$ equal to zero and solve for the radius r, we get the no-growth radius $\hat{r}$

$$\hat{r} = \frac{2\gamma V_m^p}{RT}\left[\ln\left(\frac{C_m}{C_m^e}\right)\right]^{-1}. \tag{24}$$

We claim that if the system is not in equilibrium then this no-growth radius $\hat{r}$ is only equal to the critical radius r^* under the following assumptions:

1. The elements within the system are considered to be of equal molar mass, or equivalent that $x_m/x_m^e = C_m/C_m^e$ holds, in Eq. (17).
2. The precipitates consist of a single solute element, that is $x_p \equiv 1$.
3. The free energy ΔG is solely influenced by the chemical volume free energy and the surface energy.

We claim that in all other cases $\hat{r} \neq r^*$ will hold. This claim is sustained by the analysis in A.

3. Numerical methods

3.1. Elastic deformation

To solve the system in Eq. (4), we apply the basic finite-element method on these equations, adapted to the cylindrical region. After eliminating the dependency on θ due to rotation symmetry, the (η, z)-domain is discretized using linear triangles and line elements. This method consists of multiplying Eqs. (4a) and (4b) by v_η respectively v_z, which are set equal to zero on Γ_1 respectively on Γ_2 and integrating by parts to minimize the order of spatial derivatives over the domain Ω.

The resulting system can be cast in the form using Newton–Cotes integration and the divergence theorem

$$\begin{bmatrix} S_{\eta\eta} & S_{\eta z} \\ S_{z\eta} & S_{zz} \end{bmatrix} \begin{bmatrix} \boldsymbol{u}_\eta \\ \boldsymbol{u}_z \end{bmatrix} = \begin{bmatrix} \boldsymbol{q}_\eta \\ \boldsymbol{q}_z \end{bmatrix}, \tag{25}$$

from which the values of $\boldsymbol{u}_\eta$, $\boldsymbol{u}_z$ can be solved. Using the same finite-element approach on the definitions of the strains, Eq. (6), the system

$$\begin{bmatrix} \Lambda & & & \\ & \Lambda & & \\ & & \Lambda & \\ & & & \Lambda \end{bmatrix} \begin{bmatrix} \varepsilon_{\eta\eta} \\ \varepsilon_{\theta\theta} \\ \varepsilon_{zz} \\ \varepsilon_{\eta z} \end{bmatrix} = \begin{bmatrix} 2U_\eta & \\ U_\theta & \\ & 2U_z \\ U_z & U_\eta \end{bmatrix} \begin{bmatrix} \boldsymbol{u}_\eta \\ \boldsymbol{u}_z \end{bmatrix}, \tag{26}$$

can be derived. After solving this system, the stresses can be calculated using Eq. (5) and subsequently the elastic strain energy density Δg_s^{el} using Eq. (9). The symbols $S_{[\cdot]}$, $\mathbf{q}_{[\cdot]}$, Λ and $U_{[\cdot]}$ are matrices which result from the application of the finite-element method.

3.2. Nucleation and growth

As mentioned in Section 2, the differential equation in Eq. (1) is discretized using the first-order upwind method in the particle radius domain. If a number of n_n points is chosen in the particle radius domain, let $\boldsymbol{N}$ be a column vector containing the n_n unknowns, then Eq. (1) is transformed into

$$\frac{\partial \boldsymbol{N}}{\partial t} = A\boldsymbol{N} + \boldsymbol{S} \tag{27}$$

The $n_n \times n_n$ matrix A, which is a nonlinear function of $\boldsymbol{N}$, and column vector $\boldsymbol{S}$ of length n_n, which is a nonlinear function of r, t and $\boldsymbol{N}$, are defined as:

$$A_{i,i-1}(\boldsymbol{N}) = \frac{1}{\Delta r_i} v^+_{i-1/2}(\boldsymbol{N}) \qquad \text{for } i = 2, \ldots, n_n, \tag{28a}$$

$$A_{ii}(\boldsymbol{N}) = -\frac{1}{\Delta r_i} v^-_{i-1/2}(\boldsymbol{N}) - \frac{1}{\Delta r_i} v^+_{i+1/2}(\boldsymbol{N}) \qquad \text{for } i = 1, \ldots, n_n, \tag{28b}$$

$$A_{i,i+1}(\boldsymbol{N}) = \frac{1}{\Delta r_i} v^-_{i+1/2}(\boldsymbol{N}) \qquad \text{for } i = 1, \ldots, n_n - 1, \tag{28c}$$

$$S_i(r, t, \boldsymbol{N}) = S(r_i, t, \boldsymbol{N}) \qquad \text{for } i = 1, \ldots, n_n. \tag{28d}$$

In these equations the plus and minus signs refer to the positive respectively the negative part of a number. The positive part and negative part of a number a are defined as

$$a^+ = \max(a, 0), \qquad a^- = -\min(a, 0). \tag{29}$$

In this study we use a third order time integration method from Norsett and Thomsen [16], similar to Robson [20], although Robson [20] does not specify which method is used. The method we will apply is an Embedded Singly Diagonally Implicit Runge–Kutta (ESDIRK) method. This method is best described by using a Butcher tableau (see [12]), which can be found in Table 2. One time step from t^n to t^{n+1} is performed by solving the three systems

$$\boldsymbol{k}_i = A\left[\boldsymbol{N}^n + \sum_{j=1}^{i-1} a_{ij}\Delta t \boldsymbol{k}_j\right] \cdot \left(\boldsymbol{N}^n + \sum_{j=1}^{i} a_{ij}\Delta t \boldsymbol{k}_j\right) + \boldsymbol{S}\left[t^n + \sum_{j=2}^{3} \delta_{ij} c_j \Delta t, \boldsymbol{N}^n + \sum_{j=1}^{i-1} a_{ij}\Delta t \boldsymbol{k}_1\right] \qquad \text{for } i = 1, 2, 3, \tag{30}$$

Table 2
Butcher tableau of the used ESDIRK-method.

		a		
	$\frac{5}{6}$	$\frac{5}{6}$	0	0
c	$\frac{29}{108}$	$-\frac{61}{108}$	$\frac{5}{6}$	0
	$\frac{1}{6}$	$-\frac{23}{183}$	$-\frac{33}{61}$	$\frac{5}{6}$
	b	$\frac{25}{61}$	$\frac{36}{61}$	0
	e	$\frac{26}{61}$	$\frac{324}{671}$	$\frac{1}{11}$

in which $A[\cdot]$ and $\boldsymbol{S}[\cdot,\cdot]$ are the functions as defined in Eq. (31b). The three solutions k_i, $i = 1, 2, 3$ are then substituted into

$$\boldsymbol{N}^{n+1} = \boldsymbol{N}^n + \sum_{i=1}^{3} b_i \Delta t \boldsymbol{k}_i, \tag{31a}$$

$$\widetilde{\boldsymbol{N}}^{n+1} = \boldsymbol{N}^n + \sum_{i=1}^{3} e_i \Delta t \boldsymbol{k}_i, \tag{31b}$$

giving a third and a fourth order accurate solution.

From the vectors $\boldsymbol{N}^{n+1}$, $\widetilde{\boldsymbol{N}}^{n+1}$ an approximation of the local truncation error can be computed:

$$\tau^{n+1} = \left\| \boldsymbol{N}^{n+1} - \widetilde{\boldsymbol{N}}^{n+1} \right\|_\infty. \tag{32}$$

This approximation is used to determine whether $\boldsymbol{N}^{n+1}$ is accepted or rejected by comparison with a tolerance parameter `TOL`m defined as:

$$\texttt{TOL} = \text{percentage} \cdot \left\| \mathbb{N}^{n+1} \right\|_\infty. \tag{33}$$

In the first case the time step is increased and we advance to the next iteration, in the latter case the size of the time step is decreased and we recompute the last iteration. This method is summarized in Algorithm 1. The parameters α, β, `TOL`, `maxiter` and `startvalue` are set by the user.

Algorithm 1. Adaptive time step algorithm.

set `iter` =1
set Δt= `startvalue`
while `iter` <`maxiter`
1. **compute** N^{n+1}
2. **compute** $\widetilde{N}^{n+1}$
3. **compute** τ^{n+1}
   if $\tau^{n+1} > \beta \cdot$ `TOL`
      reject N^{n+1}
      set $\Delta t = \Delta t/2$
   else if $\tau^{n+1} >$ `TOL`
      accept N^{n+1}
      set $\Delta t = \Delta\ t \cdot 0.9 \cdot (\texttt{TOL}/\tau^{n+1})^{1/2}$
      set `iter` = `iter` +1
   else if $\tau^{n+1} >$ `TOL`$/\alpha$
      accept N^{n+1}
      set `iter`= `iter` +1
   else
      accept N^{n+1}
      set $\Delta t = \Delta\ t \cdot 0.9 \cdot (\texttt{TOL}/\tau^{n+1}/\alpha)^{1/2}$
      set `iter` = `iter` +1
   end(if)
end(while)

In this paper we will only focus on the local influence of the elastic deformation on the nucleation and growth of precipitates, therefore no interpolation is performed over the computational domain. If this is preferred, other models should be incorporated which describe the spatial correlations due to diffusion of cobalt through the matrix. Instead we will use Algorithm 1 with various values as input for Δg_s^{el} which are resulting from an application of the model for elastic deformation.

To combine the two models, we propose a straightforward algorithm, to compute the effect of elastic deformation on the process of nucleation and growth of particles. This algorithm determines the value of the elastic strain energy density throughout the entire domain and determines a predefined set of points. Then for each point the results of the process of nucleation and growth of precipitates

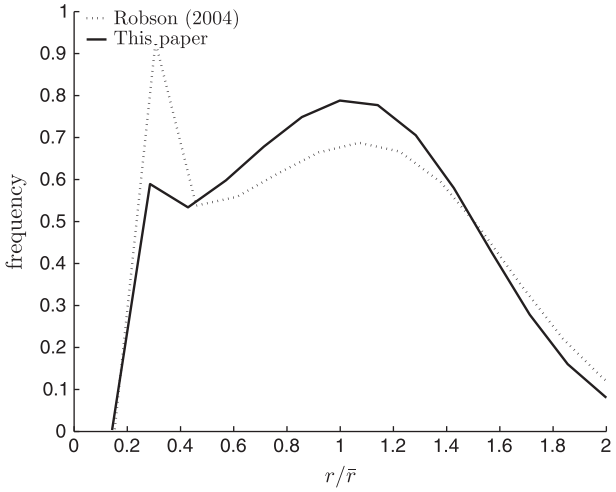

(a) $t \approx 10^2$ s, $\bar{r} \approx 1.4$ nm.

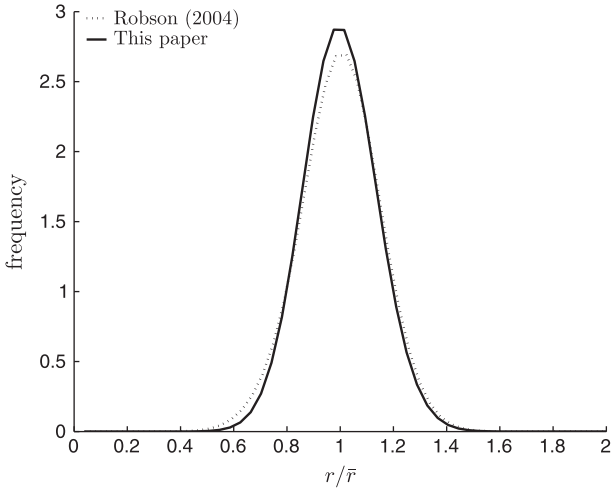

(b) $t \approx 10^3$ s, $\bar{r} \approx 5.1$ nm.

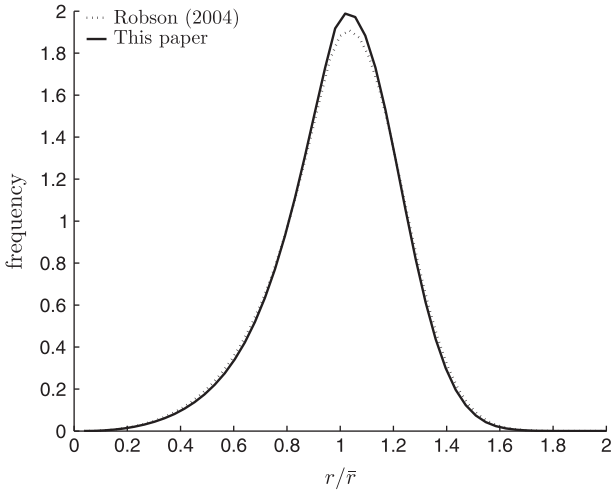

(c) $t \approx 10^4$ s, $\bar{r} \approx 5.3$ nm.

Fig. 2. Sample particle size frequency distributions both for our model and for the model proposed by Robson [20] for Cu–0.95 wt%Co at 600 °C.

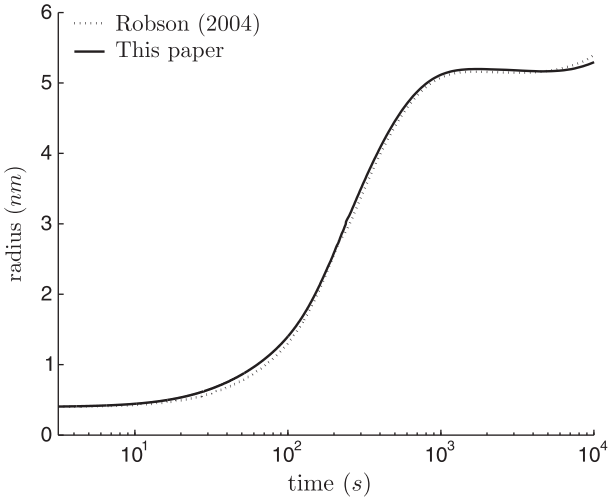

(a) Mean particle radius.

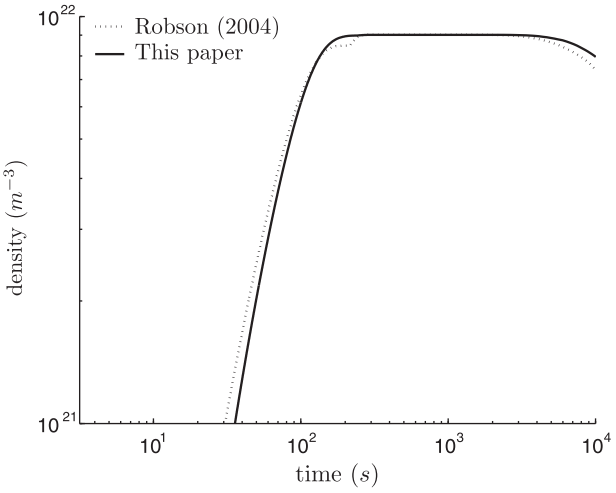

(b) Particle number density.

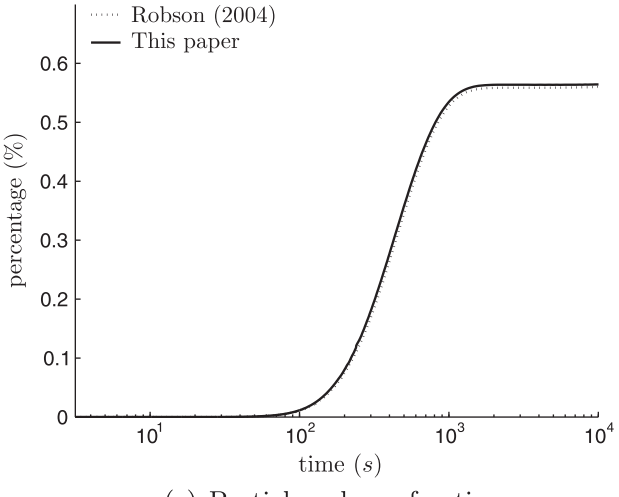

(c) Particle volume fraction.

Fig. 3. Comparison simulations for Cu–0.95 wt%Co at 600 °C.

are computed. This computation is an altered form of Algorithm 1, which computes the results at the discrete times resulting from an application of Algorithm 1 with no elastic deformation.

The above used numerical methods are mass conserving up to an accuracy of tenths of percents of the initial mass of the system independent of the parameters used in Algorithm 1.

4. Results

This section will present the results of various simulations. First we will compare the results from the present model with those obtained with the model by Robson [20] in the absence of elastic deformations. Next a tension test is simulated, from which the results will be used in simulations to investigate the effects of elastic deformations, changes in temperature and the interfacial energy.

4.1. Reference simulation

To investigate the influence of elastic deformation on the nucleation and growth of particles, first a reference situation should be provided in which no elastic deformation is assumed. As reference results we use those of Robson [20], but computed with our model. As the model by Robson [20] does not incorporate the misfit strain energy density, the value for the interfacial energy, 0.219 J/m^2, in the model by Robson [20] is higher then the value for the interfacial energy, 0.1841 J/m^2, used in our model. The value by of 0.219 J/m^2 is derived in Stowell [26] under the assumption that

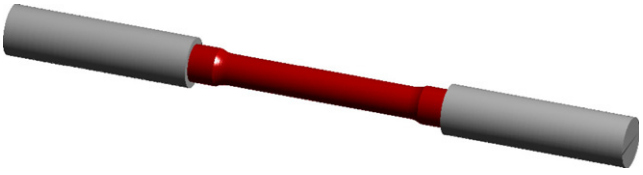

(a) Shape of the simulated specimen.

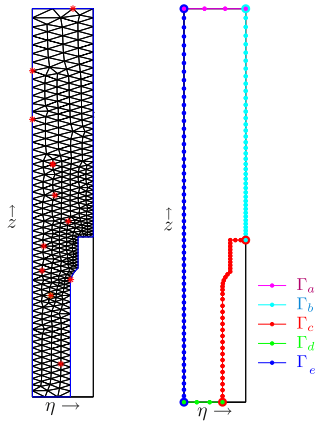

(b) The mesh. (c) The boundaries.

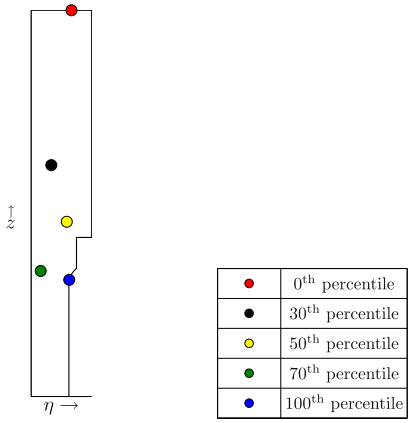

(d) Location of used percentiles at 600 °C.

	0^{th} percentile
	30^{th} percentile
	50^{th} percentile
	70^{th} percentile
	100^{th} percentile

(e) Legend with Figure 4(d) .

Fig. 4. Orientation of the used finite-element mesh and corresponding elements.

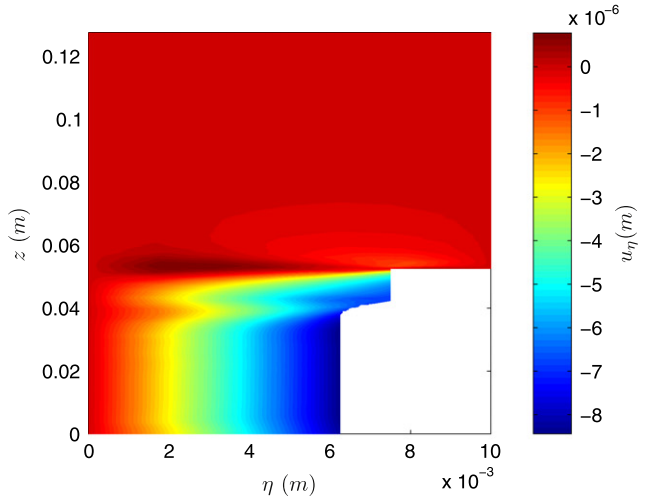

(a) Radial displacement u_η.

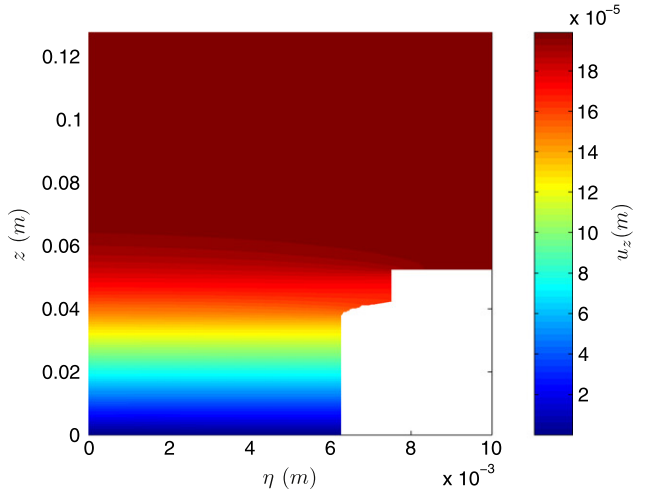

(b) Axial displacement u_z.

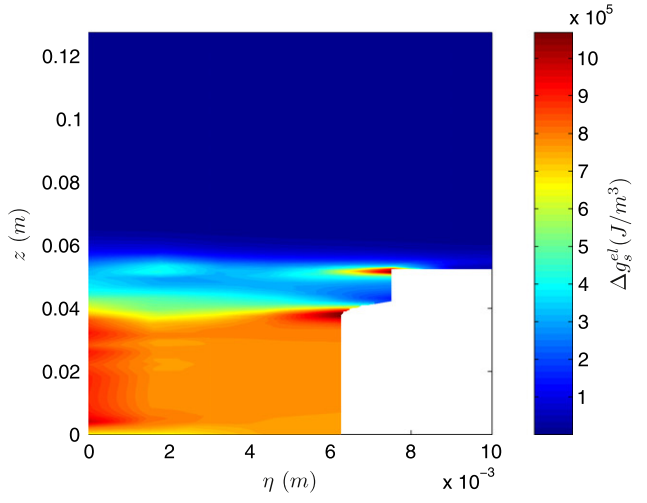

(c) Elastic strain energy density Δg_s^{el}.

Fig. 5. Results of tensile test simulation of 550 MPa.

no misfit occurs. This has as a result that the derived value of 0.219 J/m^2 is higher due to compensation for the neglection of misfit, where the value 0.1841 J/m^2 includes no compensation for misfit strain energy, as misfit is taken directly into account in the present model.

The composition of the Cu–Co system simulated is 1.02 at%Co, or equivalent 0.95 wt%Co, with the remainder Cu and the simulation was performed using a temperature of 600 °C. The percentage used in the level of tolerance, Eq. (33), during the use of Algorithm 1 is taken as 10^{-5}, the domain of the radii simulated runs from 10^{-10} to 4.98×10^{-8} m, divided in size classes of 2×10^{-10} m. The parameters α and β of Algorithm 1 are taken as 2 and 1.5.

To depict the behavior of N as a function of time we have taken snapshots of this distribution at times around 10^i, $i = 2, 3, 4$ s, as seen in Fig. 2. The plotted frequencies $f(x)$ fullfil the criteria

$$\int_{-\infty}^{\infty} f(x)\,dx = 1, \tag{34}$$

where x is defined as $r/\bar{r}$. From these figures it appears that the qualitative and quantitative behavior of the present model and the model by Robson [20] are the close to similar at these moments. The time development of some average properties for both simulations are shown in Fig. 3. These pictures again show the same qualitative and quantitative behavior, from which we can conclude that the neglection of the misfit strain energy density Δg_s^m and the use of the number of potential nucleation sites N_v in the model by Robson [20] causes a higher value of the misfit strain energy to obtain correct results. As a consequence, the incorporation of the misfit strain energy and by not using the number of potential nucleation sites as a fitting parameter in the present model predict a reasonable value for the interfacial energy. Furthermore is the present model less prone to fitting problems, as the number of fitting parameters is restricted to a single one, namely the interfacial energy.

Fig. 3 also shows that the process of nucleation, growth and coarsening of precipitates for this system can be divided into three distinct periods of time. The first period runs up to about 10^2 s and mainly contains nucleation of new precipitates. After this nucleation period, the nucleation rate drops to zero and a period of growth is achieved, which results in an increase of the mean particle radius and a constant particle number density. Next a period of coarsening is achieved, which starts at about 10^3 s, causing at first a constant mean particle radius, but eventually the number of small particles decreases, whereas larger particles grow. This causes the particle number density to drop and the mean particle radius to increase.

4.2. Tensile test

To investigate the performance of our proposed model under elastic deformation, we simulate a uniaxial tensile test on a specimen of the ASTM Standard E8M (2001e2) [2], page 6, as in Fig. 4a with a finite-element mesh as in Fig. 4b. This finite-element mesh is generated using the finite-element package SEPRAN [23]. The specimen is assumed to be clamped on both ends over the full range. The clamps are pulled upward respectively downward with the same displacements, these displacements are assumed to be constant over the clamped regions. The surface of the specimen can be divided into three regions:

$$\Gamma_a = \text{Top of the specimen}, \tag{35a}$$
$$\Gamma_b = \text{Clamped region}, \tag{35b}$$
$$\Gamma_c = \text{Indented region}. \tag{35c}$$

Let the boundary Γ_d be defined as:

$$\Gamma_d = \{(\eta, z) | z = 0\}, \tag{35d}$$

and the boundary Γ_e be defined as:

Table 3
Used values for combined simulations.

Percentile	Energy density (J/m^3)
0th	2.5031×10^{-4}
30th	4.5796×10^{2}
50th	7.3062×10^{4}
70th	5.0720×10^{5}
100th	1.0734×10^{6}

$$\Gamma_e = \{(\eta, z) | \eta = 0\}, \tag{35e}$$

which arise from the symmetrical pulling upward and downward and the boundary condition from the assumption of rotation symmetry. These five boundaries are depicted in Fig. 4c. The essential and natural boundaries from Eq. (8) are given by

$$\Gamma_{\text{ess},\eta} = \Gamma_b \cup \Gamma_e, \tag{36a}$$
$$\Gamma_{\text{nat},\eta} = \Gamma_a \cup \Gamma_c \cup \Gamma_d, \tag{36b}$$
$$\Gamma_{\text{ess},z} = \Gamma_b \cup \Gamma_d, \tag{36c}$$
$$\Gamma_{\text{nat},z} = \Gamma_a \cup \Gamma_c \cup \Gamma_e. \tag{36d}$$

Furthermore the value of f_η is zero at $\Gamma_{\text{nat},\eta}$, f_z is zero at $\Gamma_{\text{nat},z}$. The value of u_η^* from Eq. (8) is taken zero along $\Gamma_{\text{ess},\eta}$. The value of u_z^* is taken as zero along $\Gamma_{\text{ess},z}$, except for points belonging to Γ_b, where the value

$$u_z^* = 2 \times 10^{-4}\ \text{m},$$

is used, which results in Von Mises stresses below 550 MPa in the material following the Von Mises yield criterion (see [9], Chapter 3). A typical set of displacements and resulting strain energy density can be seen in Fig. 5. We stress that the resulting displacements, strains and stresses are likely beyond the elastic region of the copper-system, but they remain relevant if one considers a general mechanical energy density due to external stresses. If we assume that all elastic energy from Fig. 5c is converted to energy stored in dislocations, a simple calculation shows that at most a dislocation density of 10^{15} per cubic meter is achieved. As this is a maximum, we can safely assume that the values obtained under continuous elasticity, are presentative for mechanical energy due to external forces.

4.3. Combined model

4.3.1. Influence of strain energy at a single temperature

To investigate the influence of the elastic strain energy density originating from the tensile test simulation on the model for nucleation and growth of precipitates at the constant temperature of 600 °C, the adapted form of Algorithm 1 is applied with the values taken as the 0th, 30th, 50th, 70th and 100th percentile[3] of the results from Fig. 5(c), including the minimum and maximum of the elastic strain energy density. The grid points corresponding to these percentiles are marked in Fig. 4b and the corresponding energy levels can be found in Table 3. The results depicting the time evolution of various variables as functions of various energy levels can be seen in Figs. 6. These results are shown as the relative differences between the results from applying the specified amount of elastic energy and the results in the absence of elastic energy from Fig. 3. If $f(\Delta g_s^{el}, T, \gamma)$ is a result of simulations at elastic strain energy density Δg_m^{el}, temperature T and interfacial energy γ, the relative differences in percentages for these results are defined as

[3] The Xth percentile of a data set is defined as the value below which X percent of the data falls.

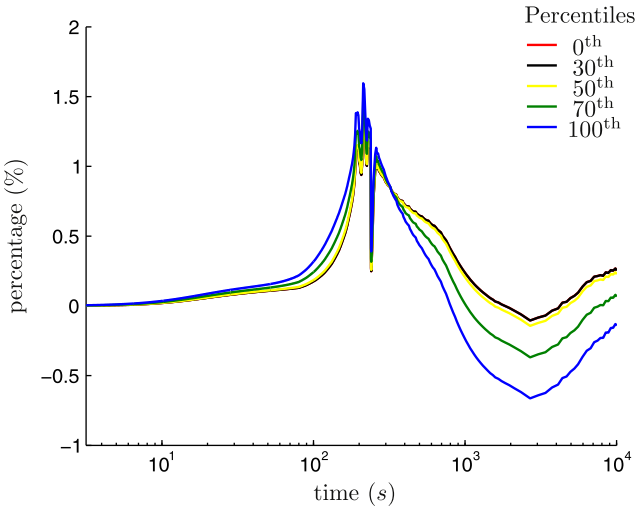

(a) Mean particle radius.

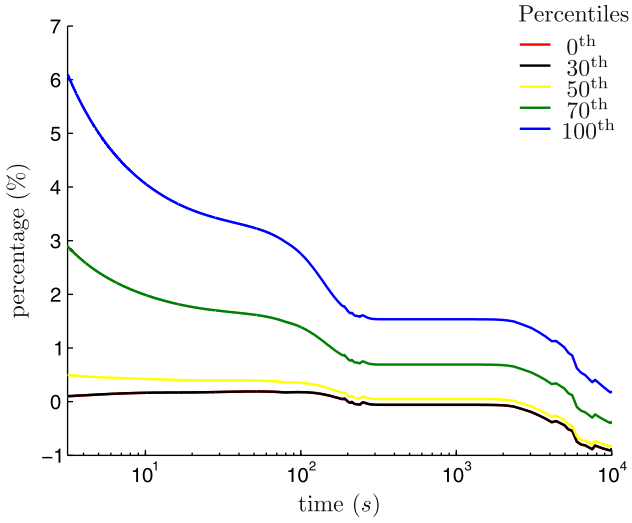

(b) Particle number density.

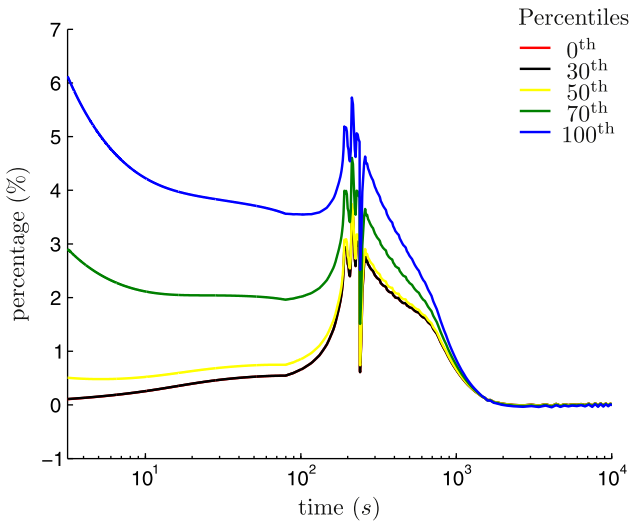

(c) Particle volume fraction.

Fig. 6. Results of combined simulation. Results are percentual differences with results from absence of elastic deformation. The value of the elastic strain energy density for each percentile can be found in Table 3.

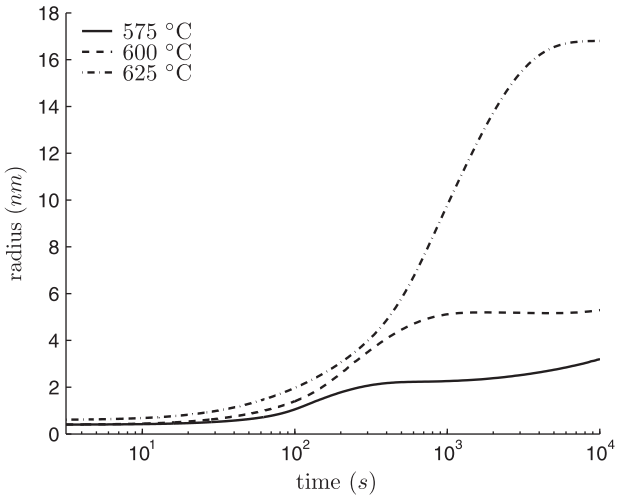

(a) Mean particle radius.

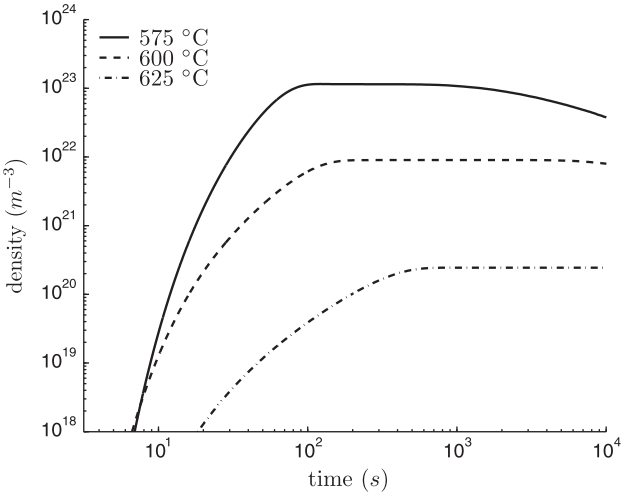

(b) Particle number density.

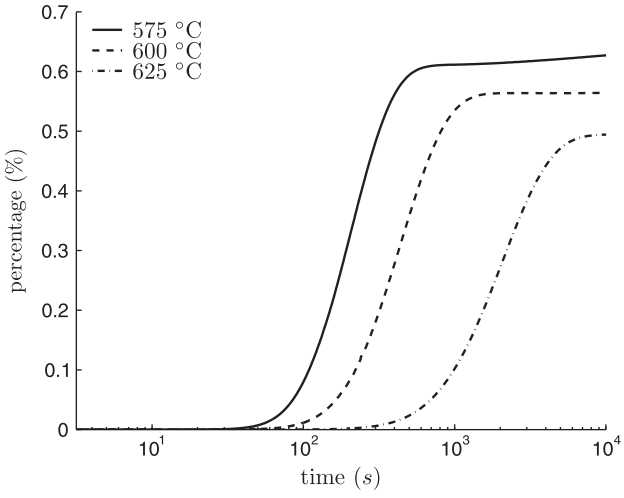

(c) Particle volume fraction.

Fig. 7. Result of simulations for Cu–0.95 wt%Co at 575, 600 and 625 °C.

$$\frac{f(\Delta g_s^{el}, T, \gamma) - f(0, T, \gamma)}{f(0, T, \gamma)} \times 100\%. \tag{37}$$

From the results in Fig. 6, we can see that the mean particle radius, the particle number density and the particle volume fraction show a clear correlation with the strain energy density as in Fig. 5c and the used values in Table 3. We can also see that incorporating strain energy from elastic deformation increases the mean particle radius slightly and the particle number density significantly during the nucleation period, causing a larger particle volume fraction. This causes lower growth rates due to Eq. (22) and as a result a decreasing mean particle radius during the growth period. Eventually the mean particle radius will increase due to coarsening of the precipitates, but will remain close to the mean particle radius in the absence of elastic displacements. The influence of the incorporation of the elastic strain energy can also clearly be seen in the results from the particle number density. As this density is higher with respect to the reference results, see Fig. 3b, during the nucleation and growth period, at the onset of the coarsening period relatively more small precipitates will be present. This causes a quicker decrease in the number density in the coarsening period itself, with an eventual value close to the results from the reference simulation.

4.3.2. Influence of strain energy and temperature

To investigate the influence of elastic strain energy at different temperatures, we will first run Algorithm 1 at constant temperatures of 575, 600 and 625 °C, in the absence of elastic deformation, using the values of all parameters as stated in Table 1 and previously. The results from these simulations can be seen in Fig. 7.

From Fig. 7 various effects of changing the temperature can be seen. The first effects are that at higher temperatures larger, but fewer precipitates are formed and the solubility of cobalt increases, as can be expected from the used exponential relationship between temperature and the equilibrium concentration of cobalt in Eq. (23). A closer inspection of the results shows also that the length of the nucleation period and the length of the growth period increase with increasing temperature.

Next three points are taken from the finite-element grid as in Fig. 4d, for which at each temperature of the three temperatures the resulting elastic strains are calculated. These values can be found in Table 4. The three chosen points correspond to the minimum, the maximum and the 70th percentile of the elastic strain energy density from simulations at 600 °C. For these three points simulations are run at the three temperatures of 575, 600 and 625 °C. The results from these simulations are shown in Fig. 8 for each temperature as the relative differences between the results from applying the specified amount of elastic energy and the results in the absence of elastic energy from Fig. 7 at that temperature in percentages. The relative differences are defined as in Eq. (37).

The results in Fig. 8 show that for each simulated temperature again the relative differences of the mean particle radius, particle number density and the particle volume fraction are closely related to the magnitude of the used elastic strain energy density. With respect to the dependency of the results on the temperature, we see that at each temperature the same qualitative behavior is observed, but with a shift in the temporal domain. This shift can be

Table 4
Used elastic strain energy density values (J/m^3) for temperature influence simulations.

Point	Temperature (°C)		
	575	600	625
Min	2.5257×10^{-4}	2.5031×10^{-4}	2.4805×10^{-4}
70th	5.0702×10^{5}	5.0720×10^{5}	4.9794×10^{5}
Max	1.0831×10^{6}	1.0734×10^{6}	1.0637×10^{6}

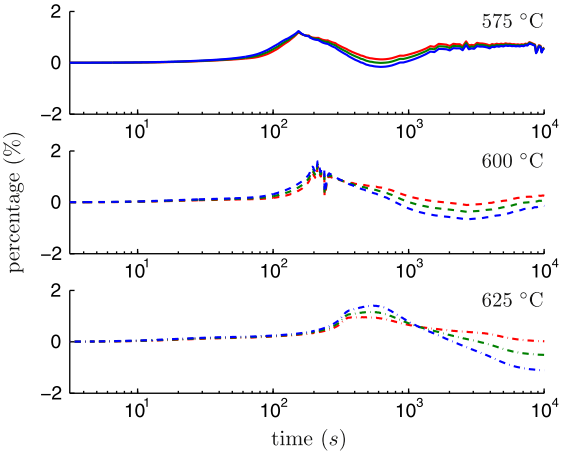

(a) Mean particle radius.

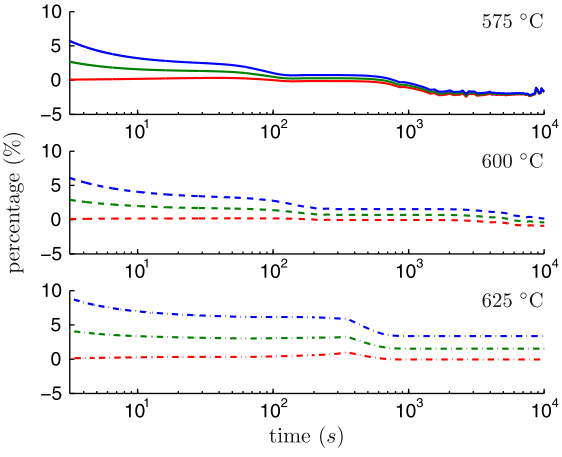

(b) Particle number density.

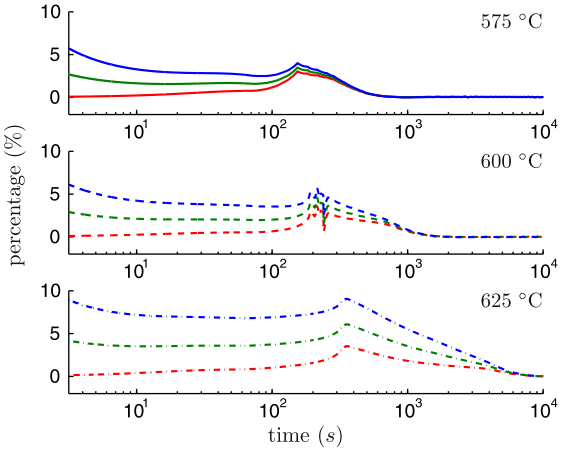

(c) Particle volume fraction.

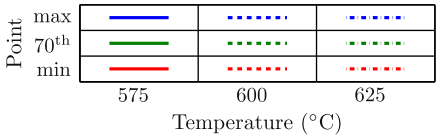

(d) Legend.

Fig. 8. Result of simulations for Cu–0.95 wt%Co at 575, 600 and 625 °C for the elastic strain energy densities from Table 4.

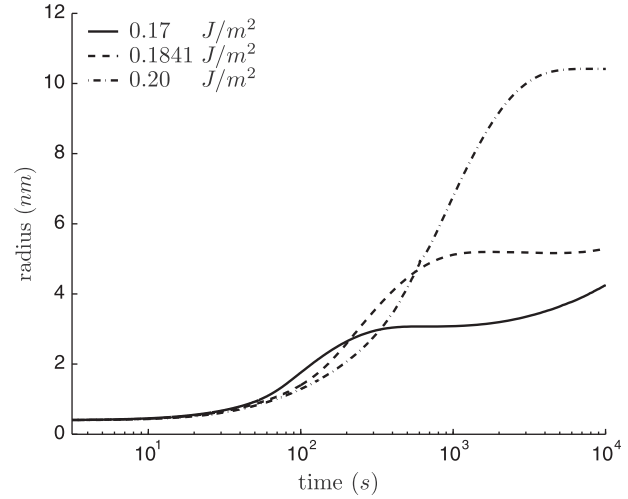

(a) Mean particle radius.

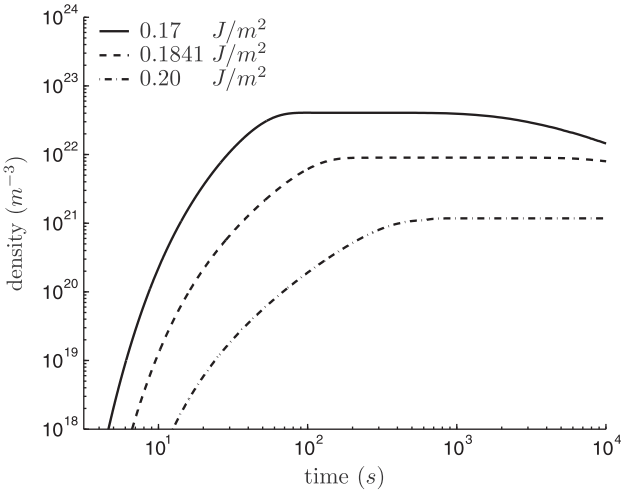

(b) Particle number density.

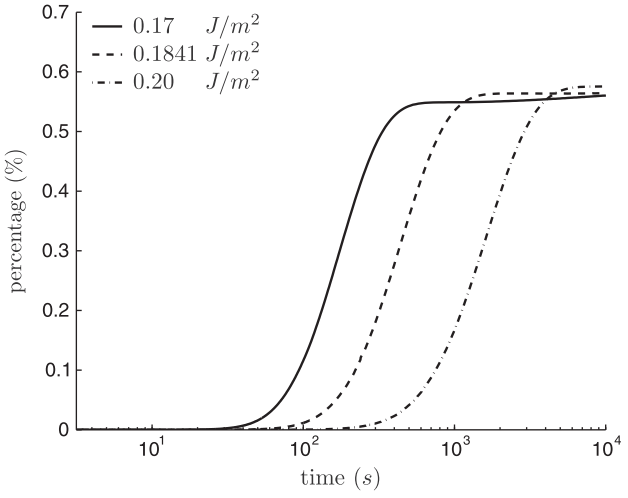

(c) Particle volume fraction.

Fig. 9. Results of simulations for Cu–0.95 wt%Co at 600 °C with values of 0.17, 0.1841 and 0.20 J/m^2 for the interface energy.

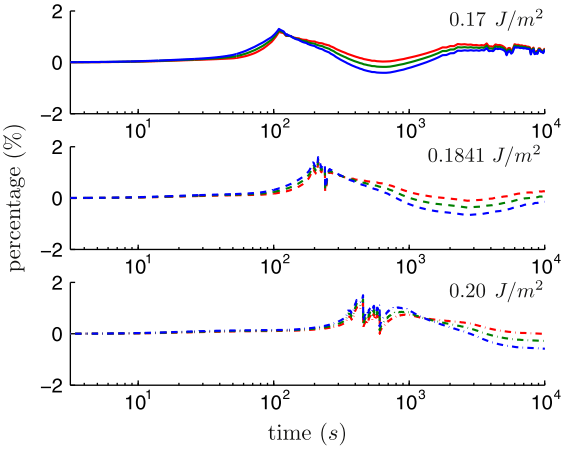

(a) Mean particle radius.

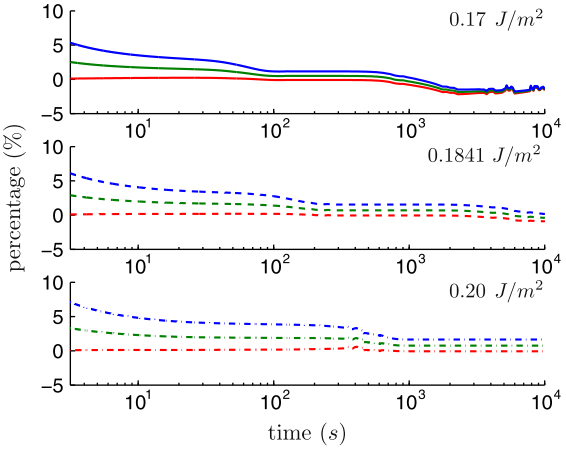

(b) Particle number density.

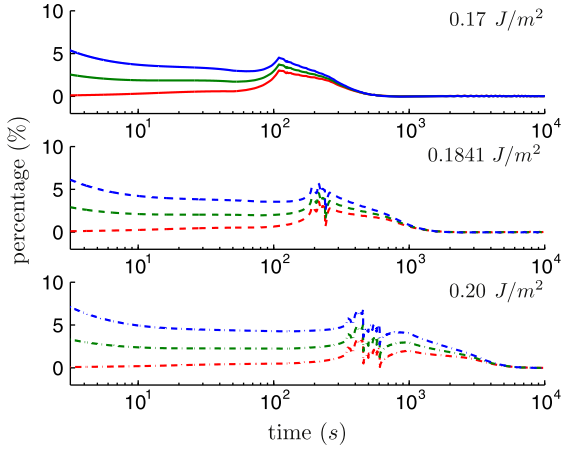

(c) Particle volume fraction.

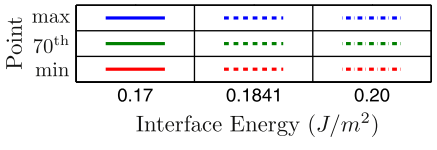

(d) Legend.

Fig. 10. Results of simulations for Cu–0.95 wt%Co at 600 °C for three of the elastic strain energy densities from Table 3 with values of 0.17, 0.1841 and 0.20 J/m^2 for the interface energy.

explained by comparing the results in Fig. 7 with those in Fig. 8. From the particle number density we see for on increasing temperature a later start of the growth period and a longer growth period (Fig. 7a), which can also be seen in Fig. 8 as a shift in the characteristics of the relative differences for each variable shown. Fig. 8 shows that with increasing temperature the relative differences due to the elastic strain energy densities increases. We can conclude that the main differences between the results at various temperatures are mostly caused by changes in the behavior of the system due to the temperature itself, although a slight increased effect of incorporating the elastic strain energy can be seen at higher temperatures.

4.3.3. Influence of strain energy and interface energy

To investigate the influence of elastic strain energy at different values of the interface energy γ, we will first run Algorithm 1 at a constant temperature of 600 °C with the fitted value of 0.1841 J/m^2 and the values of 0.17 and 0.20 J/m^2, in the absence of elastic deformation, using the values of all other parameters as stated in Table 1 and previously. The results from these simulations can be seen in Fig. 9.

Although the results for different values of the interface energy (Fig. 9) are similar in nature to the values obtained for multiple temperatures (Fig. 7), at some points differences occur. One of these differences is the fact that increasing the interface energy does not influence the solubility. Due to this the growth period will remain the same, although the growth rates should be influenced by an increased interface energy. On inspection of the growth rates and it's dependency on the interface energy, only a large positive influence of the growth rate is seen for small precipitates. As the system predicts on average larger precipitates due to an increase in interface energy, these higher growth rates are negligible.

Next three points are taken from the finite-element grid as in Fig. 4d, for which the resulting elastic strains can be found in Table 3. The three chosen points correspond to the minimum, the maximum and the 70th percentile of the elastic strain energy density from the simulations at 600 °C. For these three points simulations are performed with the values of 0.1841 J/m^2 and the values of 0.17 and 0.20 J/m^2 for the interface energy. The results from these simulations are shown in Fig. 10 for each value of the interface energy as the relative differences between the results from applying the specified amount of elastic energy and the results in the absence of elastic energy from Fig. 9 at that value of the interface energy. The relative differences are defined as in Eq. (37).

Similar to the results in Fig. 8 for the various temperatures, the results in Fig. 10 show a clear correlation with the value of the interface energy. The shift of the qualitative behavior in the temporal domain is again present, and coincides with the effects of changing the value of the interface energy in the absence of elastic deformation. We can conclude that the main differences between the results at various values of the interface energy are mostly caused by changes in the behavior of the system due to the interface energy itself, although a slight increased effect of incorporating the elastic strain energy can be seen at higher values of the interface energy.

5. Conclusions

In this paper we have combined a model for the nucleation and growth of particles in a binary alloy with elastic deformations from a uniaxial tensile test. This model has been implemented using both finite-volume and finite-element methods. The simulation concerns a binary copper-cobalt alloy at fixed temperatures during a hypothetical uniaxial tensile test. The results from the simulations show that incorporation of strain energy due to elastic deformation promotes the nucleation of precipitates with an initially larger mean radius, but an eventual smaller mean particle radius due to faster depletion of the matrix. The results for simulations at different temperatures and different values of the interface energy, show that the influence of elastic deformations on the process of nucleation and growth of precipitates is mainly restricted to a quantitative effect, where the effect increases with increasing values of the elastic strain energy density. These results also show that both a higher (lower) temperature and interface energy cause larger (smaller) and more (less) precipitates during the initial stages of the process. The effect of a higher (lower) temperature will remain during the entire process as the solubility changes, where the effect of a higher (lower) interface energy decays as the solubility does not changes.

Acknowledgement

This research was carried out under the Project Number M41.5.09341 in the framework of the Research Program of the Materials innovation institute M2i (www.m2i.nl).

Appendix A. Proof of claim

In Section 2.2.2 we claimed that if the system is not in equilibrium then the no-growth radius $\hat{r}$ (Eq. (24)) is only equal to the critical radius r^* (Eq. (15)) under the following assumptions:

1. The elements within the system are considered to be of equal molar mass, or equivalent that $x_m/x_m^e = C_m/C_m^e$ holds, in Eq. (17).
2. The precipitates consist of a single solute element, that is $x_p \equiv 1$.
3. The free energy ΔG is solely influenced by the chemical volume free energy and the surface energy.

We claimed that in all other cases $\hat{r} \neq r^*$ will hold.

To prove our claims assume 1–3 as stated above. Assumptions 1 and 2 cause Eq. (17) to become

$$\Delta g_v = \frac{RT}{V_m^p} \ln\left(\frac{C_m}{C_m^e}\right). \tag{A.1}$$

Using Eq. (15) and assumption 3, we obtained

$$r^* = \frac{2\gamma V_m^p}{RT}\left[\ln\left(\frac{C_m}{C_m^e}\right)\right]^{-1}, \tag{A.2}$$

which is identical to Eq. (24), proving that under assumptions 1–3 $r^* = \hat{r}$.

To prove the uniqueness of $r^* = \hat{r}$ under the three assumptions, note that $r^* = \hat{r}$ should fail if at least one of the assumptions is violated. For each of the seven possible combinations of failed assumptions below is a proof stated that $r^* \neq \hat{r}$.

Case I – Only assumption 1 is violated: Due to assumption 2, we have

$$\Delta g_v = \frac{RT}{V_m^p} \ln\left(\frac{x_m}{x_m^e}\right). \tag{A.3}$$

This can be rewritten as

$$\Delta g_v = \frac{RT}{V_m^p} \ln\left(\frac{C_m}{C_m^e}\right) + \frac{RT}{V_m^p} \ln\left(f(p,q)\right), \tag{A.4}$$

in which the $p = C_m/C_m^e$ and $q = M_2/M_1$, with M_2 and M_1 the molar mass of the solvent respectively the solute element, and $f(p,q)$ defined by

$$f(p,q) = \frac{(q-1)C_m^e + 100}{p(q-1)C_m^e + 100}. \tag{A.5}$$

For this function f, it can be shown that the sign of $(p-1)(q-1)$ is of importance to the value of f. If $(p-1)(q-1)$ is negative, $f(p,1)$ will be larger then 1, and if $(p-1)(q-1)$ is positive, $f(p,1)$ will be smaller then 1. This indicates that we must have

- If $(p-1)(q-1) > 0$, then $\Delta g_v < \frac{RT}{V_m^p}\ln(\frac{C_m}{C_m^e})$;
- If $(p-1)(q-1) < 0$, then $\Delta g_v > \frac{RT}{V_m^p}\ln(\frac{C_m}{C_m^e})$;

and as a consequence by Eq. (15)

- If $(p-1)(q-1) > 0$, then $r^* > \hat{r}$;
- If $(p-1)(q-1) < 0$, then $r^* < \hat{r}$.

which proves that if assumption 1 is violated, we cannot have $r^* = \hat{r}$.

Case II – Only assumption 2 is violated: If we apply assumption 1 we obtain

$$\Delta g_v = \frac{RT}{V_m^p} x_p \ln\left(\frac{C_m}{C_m^e}\right) + \frac{RT}{V_m^p}(1-x_p)\ln\left(\frac{100-C_m}{100-C_m^e}\right). \tag{A.6}$$

For the latter part of this equation, it can be shown that if $C_m^e > C_m$, Δg_v is positive and if $C_m^e < C_m$, Δg_v is negative. Using the fact that $0 < x_p < 1$, we have, if $C_m^e < C_m$, that

$$(1-x_p)\ln\left(\frac{C_m}{C_m^e}\right) > (1-x_p)\ln\left(\frac{100-C_m}{100-C_m^e}\right). \tag{A.7}$$

This expression can be rewritten, using Eq. (17) as

$$\frac{RT}{V_m^p}\ln\left(\frac{C_m}{C_m^e}\right) > \Delta g_v. \tag{A.8}$$

As a result, we have by Eq. (15) and (24):

$$\hat{r} < r^*. \tag{A.9}$$

Similarly if $C_m^e > C_m$, we have

$$(1-x_p)\ln\left(\frac{C_m}{C_m^e}\right) < (1-x_p)\ln\left(\frac{100-C_m}{100-C_m^e}\right). \tag{A.10}$$

Which can be rewritten, using Eq. (17) as

$$\frac{RT}{V_m^p}\ln\left(\frac{C_m}{C_m^e}\right) < \Delta g_v. \tag{A.11}$$

Hence, from Eq. (15) and (24), it follows that

$$\hat{r} > r^*. \tag{A.12}$$

The above arguments proves that if assumption 2 is violated, we cannot have $r^* = \hat{r}$.

Case III – Only assumption 3 is violated: If assumption 3 is false, and we apply assumptions 1 and 2 to Eq. (17) and (15), then we obtain:

$$r^* = \frac{2\gamma}{\frac{RT}{V_m^p}\ln\left(\frac{C_m}{C_m^e}\right) + \Delta g_0}, \tag{A.13}$$

in which Δg_0 contains all other modelled energy density terms. If Δg_0 has a negative sign, then by Eq. (15) and (24) we have that $r^* > \hat{r}$, whereas if Δg_0 has a positive sign, then we have $r^* < \hat{r}$ by the same equations. This proves that if assumption 3 is violated, we cannot have $r^* = \hat{r}$.

Case IV – Only assumptions 1 and 2 are violated: Similar to Case II, we have by failure of assumption 2

$$\ln\left(\frac{C_m}{C_m^e}\right) \neq x_p \ln\left(\frac{C_m}{C_m^e}\right) + (1-x_p)\ln\left(\frac{100-C_m}{100-C_m^e}\right). \tag{A.14}$$

By failure of assumption 1, similar as in Case I, we also have

$$\ln\left(\frac{C_m}{C_m^e}\right) \neq \ln\left(\frac{x_m}{x_m^e}\right), \tag{A.15}$$

$$\ln\left(\frac{100-C_m}{100-C_m^e}\right) \neq \ln\left(\frac{1-x_m}{1-x_m^e}\right). \tag{A.16}$$

Combination of the three inequalities above give that $r^* \neq \hat{r}$, if assumptions 1 and 2 are violated.

Case V – Only assumptions 1 and 3 are violated: Due to violation of assumption 3, we have

$$\Delta g_v \neq \Delta g_v + \Delta g_0, \tag{A.17}$$

where Δg_0 is as defined in Case III. This inequality in combination with those from Case I, we have that $r^* \neq \hat{r}$ if assumptions 1 and 3 are violated.

Case VI – Only assumptions 2 and 3 are violated: Due to violation of assumption 3, we have

$$\Delta g_v \neq \Delta g_v + \Delta g_0, \tag{A.18}$$

where Δg_0 is as defined in Case III. This inequality in combination with those from Case II, we have that $r^* \neq \hat{r}$ if assumptions 2 and 3 are violated.

Case VII – Assumptions 1–3 are violated: Due to violation of assumption 3, we have

$$\Delta g_v \neq \Delta g_v + \Delta g_0, \tag{A.19}$$

where Δg_0 is as defined in Case III. This inequality in combination with those from Case IV, we have that $r^* \neq \hat{r}$ if all three assumptions are violated.

If we denote by E the equivalence of r^* and $\hat{r}$, and by $A1$, $A2$, $A3$ assumptions 1–3, it can be proven that Cases I, IV, V and VII together proof that $\neg A1 \rightarrow \neg E$, that Cases II, IV, V and VII together proof that $\neg A2 \rightarrow \neg E$ and that Cases III, V, VI and VII together proof that $\neg A3 \rightarrow \neg E$. Furthermore, using Theorem 2.2.3 of Burris [5], we can show that

$$(\neg A1 \rightarrow \neg E) \wedge (\neg A2 \rightarrow \neg E) \wedge (\neg A3 \rightarrow \neg E), \tag{A.20}$$

is equivalent with

$$E \rightarrow (A1 \wedge A2 \wedge A3). \tag{A.21}$$

Above we have proven the truth of A.20, which proves that A.21 is true, or equivalent that $r^* = \hat{r}$ implies that assumptions 1–3 hold. Together with the prove that $r^* = \hat{r}$ holds if assumptions 1–3 hold, our claim is proven.

References

[1] H.I. Aaronson, K.R. Kinsman, K.C. Russel, Scripta Metallurgica 4 (2) (1970) 101–106.
[2] ASTM Standard E8M, Standard Test Methods for Tension Testing of Metallic Materials [Metric]. ASTM International, West Conshohocken, PA, 2001e2.
[3] D.M. Barnett, J.K. Lee, H.I. Aaronson, G.F. Batalha, Scripta Metallurgica 8 (12) (1974) 1447–1450.
[4] W. Betteridge, Progress in Materials Science 24 (1980) 51–142.
[5] S.N. Burris, Logic for Mathematics and Computer Science, Prentice Hall, New Jersey, 1998.
[6] Y.A. Chang, R. Hultgren, The Journal of Physical Chemistry 69 (12) (1965) 4162–4165.
[7] K.T. Chau, X.X. Wei, International Journal of Solids and Structures 37 (40) (2000) 5707–5732.
[8] A. Deschamps, Y. Brechet, Acta Materialia 47 (1) (1999) 293–305.
[9] G.E. Dieter, Mechanical Metallurgy, third ed., McGraw-Hill, New York, 1976.
[10] R. Döhl, M.-P. Macht, V. Naundorf, Physica Status Solidi (a) 86 (1984) 603–612.
[11] T.A. Hahn, Journal of Applied Physics 41 (13) (1970) 5096–5101.
[12] W. Hundsdorfer, J.G. Verwer, Numerical Solution of Time-dependent Advection–Diffusion–Reaction Equations, Springer Series in Computational Mathematics, vol. 33, Springer-Verlag, Berlin Heidelberg, 2003.
[13] J.C. Jaeger, N.G.W. Cook, R.W. Zimmerman, Fundamentals of rock mechanics, Wiley Blackwell, 2007.
[14] R. Kampmann, R. Wagner, Materials Science and Technology – A Comprehensive Treatment, vol. 5, VCH, Weinheim, 1991.
[15] O.R. Myhr, Ø. Grong, Acta Materialia 48 (7) (2000) 1605–1615.

[16] S.P. Nørsett, P.G. Thomsen, BIT 24 (1984) 634–646.
[17] E.A. Owen, D. Madoc Jones, Proceedings of the Physical Society. Section B 67 (1954) 456–466.
[18] D.A. Porter, K.E. Easterling, Phase Transformations in Metals and Alloys, second ed., Chapmann &Hall, London, UK, 1992.
[19] N. Ratel, G. Bruno, P. Bastie, T. Mori, Acta Materialia 54 (19) (2006) 5087–5093.
[20] J.D. Robson, Materials Science and Technology 20 (2004) 441–448.
[21] H. Rolnick, Physical Review 36 (3) (1930) 506–512.
[22] K.C. Russell, Phase Transformations, American Society for Metals, Metals Park, Ohio, 1970. p. 219.
[23] G. Segal, SEPRAN Manuals, Den Haag, The Netherlands, 2010.
[24] I.S. Servi, D. Turnbull, Acta Metallurgica 14 (1966) 161–169.
[25] F. Soisson, A. Barbu, G. Martin, Acta Materialia 44 (9) (1996) 3789–3800.
[26] M.J. Stowell, Materials Science and Technology 18 (2002) 139–144.
[27] M.E. Straumanis, L.S. Yu, Acta Crystallographica Section A 25 (6) (1969) 676–682.
[28] Thermo-Calc Software AB, TCS Steel and Fe-alloys Database, 2010. <http://www.thermocalc.com/res/pdfDBD/DBD_TCFE6.pdf>.
[29] F.J. Vermolen, E. Javierre, C. Vuik, L. Zhao, S. van der Zwaag, Computational Materials Science 39 (2007) 767–774.